

# On the influence of magnetic helicity on X-rays emission of solar and stellar coronae

J. Warnecke<sup>1</sup> and H. Peter<sup>1</sup>

Max-Planck-Institut für Sonnensystemforschung, Justus-von-Liebig-Weg 3, D-37077 Göttingen, Germany  
e-mail: warnecke@mps.mpg.de

June 1, 2021, Revision: 1.5

## ABSTRACT

*Context.* Observation of solar-like stars show a clear relation between X-ray emission and their rotation. Higher stellar rotation can lead to a larger magnetic helicity production in stars.

*Aims.* We aim to understand the relation between magnetic helicity on the surface of a star to their coronal X-ray emission.

*Methods.* We use 3D MHD simulations to model the corona of the solar-like stars. We take an observed magnetogram as in photospheric activity input, and inject different values of magnetic helicity. We use synthesis emission to calculate the X-ray emission flux of each simulation and investigate how this scales with injected magnetic helicity.

*Results.* We find that for larger injected magnetic helicities an increase in temperature and an increase in X-ray emission. The X-ray emission scaled cubically with the injected helicity. We can related this to increase of horizontal magnetic field and therefore higher Poynting flux at the coronal base.

*Conclusions.* Using typical scaling of magnetic helicity production with stellar rotation, we can explain the increase of X-ray emission with rotation only by an increase of magnetic helicity at the surface of a star.

**Key words.** Magnetohydrodynamics (MHD) – Sun: magnetic fields – Sun: corona – Sun: activity – stars:activity – X-rays

## 1. Introduction

Solar-like stars show strong dependence of magnetic activity with rotation. This is most clearly seen in the enhancement of X-ray emission (e.g. Pizzolato et al. 2003; Vidotto et al. 2014; Reiners et al. 2014; Wright & Drake 2016) for increasing stellar rotation until a plateau in activity is reached. Understanding the overall relation of rotation to emission is far from trivial, because several different processes are involved: the generation and surface appearances of magnetic field and the magnetic heating in the stellar atmosphere.

Rotation is a key ingredient for the magnetic field generation below the stellar surface via a dynamo process (Brandenburg & Subramanian 2005). An increase of rotation is believed to lead to a more efficient dynamo producing larger magnetic fields. They appear at the surface in form of larger spots and heating the stellar coronae to higher temperatures, leading to higher X-ray emission. As found in solar-like stars, the integrated X-ray emission can be mostly explained via thermal radiation with a temperature to the power of  $4.5 \pm 0.3$  (Güdel 2004). This scenario is supported observationally by a clear relation between stellar rotation and the large-scale surface magnetic field (Vidotto et al. 2014). Also numerical simulations of stellar dynamos indicate a clear trend in this direction (e.g. Schrunner et al. 2014; Viviani et al. 2018; Warnecke 2018; Augustson et al. 2019; Warnecke & Käpylä 2019). Observations show further evidence for increasing coronal X-ray emission for larger magnetic surface flux (e.g. Pevtsov et al. 2003; Vidotto et al. 2014). However, the detailed process, how larger magnetic surface flux lead to higher temperatures in the stellar corona is not fully understood as in particular the small-scale granular motion play an important part in generating the necessary upward directed Poynting flux.

Beside leading to larger magnetic field via the dynamo process, stellar rotation can also influence the magnetic field topology appearing at the stellar surface. Below the surface, the interplay of convection and rotation is an essential part in the magnetic field generation via the  $\alpha$  effect (Steenbeck et al. 1966). An  $\alpha$  effect will produce helical magnetic field with a preferred handedness on the large-scales and the opposite on the small-scales (Brandenburg & Subramanian 2005) as recently confirmed to be present in the Sun (Singh et al. 2018). The helical nature of the magnetic field, expressed in terms of the magnetic helicity, depends crucially on the value of rotational influence on convection. Higher rotation lead to convective motion carrying higher helicity and therefore generating more helical magnetic fields (Krause & Rädler 1980). Therefore, one would expect that stars more rapidly rotating than the Sun shows more helical magnetic field at the stellar surface. This rotational dependence in magnetic topology in turn would also have an influence on the heating of the stellar coronae and therefore their X-ray production.

Observational studies relating magnetic helicity and X-ray emission has been limited to the work by Maeshiro et al. (2005), where they found that the X-ray flux of solar active region scales with the injection of magnetic helicity flux with a power of 1.5. However, they found a tighter correlation with the magnetic surface flux of these regions, which is more likely to be the cause of the X-ray variations. In this paper, we want to investigate how an increase of magnetic helicity at the surface changes the X-ray production of stellar coronae in-dependend on magnetic surface flux.

Magnetic helicity is a conserved quantity in ideal magnetohydrodynamics and even in the non-ideal case it decays slower than the magnetic energy (Moffatt 1978). Therefore, it is know

they play a crucial role in connecting the rotational influence magnetic field dynamics below the surface to the one above the surface. It has been shown that magnetic helicity plays a key role in the triggering of eruptive events on the Sun, e.g. solar flare and solar coronal mass ejections (e.g. [Nindos et al. 2003](#); [Pariat et al. 2017](#)). Furthermore, there are indications that magnetic helicity also plays an important role in the heating in coronal loops ([Warnecke et al. 2017](#); [Bourdin et al. 2018](#)). However, how the coronal heating scales with magnetic helicity have not been studied so far.

To measure magnetic helicity on the solar surface is not trivial. Magnetic helicity is defined as the volume integral of  $\mathbf{A} \cdot \mathbf{B}$ , involving not only the magnetic field  $\mathbf{B}$ , but also its vector potential  $\mathbf{A}$ . Hence, one needs to estimate/measure  $\mathbf{A}$  and to cope with the gauge dependency of  $\mathbf{A}$ . Commonly, the current helicity, the dot product of magnetic field and current density, is used as a proxy for magnetic helicity. It is gauge invariant and its vertical contribution can be measured from magnetograms (e.g. [Zhang et al. 2010](#)). Others invoke the gauge invariant relative helicity ([Berger & Field 1984](#)) to calculate the injection of helicity flux (e.g. [Chae et al. 2001](#); [Nindos et al. 2003](#); [Maeshiro et al. 2005](#); [Vemareddy 2019](#)) based on the photospheric motions determined by local correlation tracking. Another approach used the vector magnetograms of active region to calculate the magnetic helicity spectrum. Because this method assumes periodicity in horizontal direction it makes the obtained spectrum gauge invariant. This method was used to determine the value of magnetic helicities in several active regions ([Zhang et al. 2014, 2016](#)). They found  $10^4$  up to  $5 \times 10^5$  G<sup>2</sup>Mm for magnetic helicity density, see also the followup study by ([Gosain & Brandenburg 2019](#)). In our paper, we include various values of the magnetic helicity density at the photospheric surface and study with an established model of the solar corona ([Bingert & Peter 2011, 2013](#); [Warnecke & Peter 2019](#)), how the helicity influences the heating and X-ray production in the coronae.

The paper is structured in the following way. We first describe the basics of the numerical model including how we inject magnetic helicity in the photosphere in Section 2. Then we discuss the magnetic helicity evolution and distribution in Section 3.1, its influence on X-ray emission production in Section 3.2, and how X-ray emission, temperature and Poynting flux scales with helicity in Section 3.3. Before we conclude in Section 4, we also discuss the relation between the magnetic helicity, X-rays and extreme UV emission in Section 3.4.

## 2. Model and setup

We model the solar and stellar corona in a Cartesian box  $(x, y, z)$  starting from the photosphere ( $z=0$ ) to the corona ( $z=80$  Mm) with an horizontal extent of 100 Mm. We use the PENCIL CODE<sup>1</sup> to solve the equation of compressible resistive magnetohydrodynamics. This includes the induction equation for the vector potential  $\mathbf{A}$ , which assures the solenoidality of the magnetic field  $\mathbf{B} = \nabla \times \mathbf{A}$ , the momentum equation for the velocity  $\mathbf{u}$ , the continuity equation for  $\rho$  and equation of state for an ideal gas. The exact setup is described in detail in the work by [Bingert & Peter \(2011, 2013\)](#). The latest additions including the semi-relativistic Boris correction to the Lorentz force (e.g. [Gombosi et al. 2002](#); [Chatterjee 2018](#)) and the non-Fourier description of the heat flux evolution to speed up the calculation are presented in [Warnecke & Bingert \(2019\)](#). Key element of this model is a realistic description of the Spitzer heat conductivity, which is

along the magnetic field and depend strongly on the temperature  $T^{5/2}$ . The values of constant viscosity  $\nu$  and magnetic diffusivity  $\eta$  are chosen in such a way that their corresponding grid Reynolds numbers are around unity. This value of  $\nu$  is close to the realistic Spitzer value in the solar corona, but  $\eta$  and therefore the magnetic Prandtl number are several orders of magnitude different to realistic values. To avoid strong artificial currents and hence large ohmic heating near the top boundary we use a slightly larger value of all diffusivities and a reduced Ohmic heating term near the top boundary. We use periodic boundary conditions in the horizontal direction for all quantities. At top boundary, we use vanishing values for the velocity and heat flux with hydrostatic extrapolation for the density. The magnetic field is following a potential field extrapolation at both boundaries. At the bottom boundary, we prescribe the horizontal velocity using a granulation driver, which mimics the photospheric velocities of the Sun ([Gudiksen & Nordlund 2002](#); [Bingert & Peter 2011](#)). Temperature and density are fixed at the bottom boundary. One important ingredient of this model is that we drive the simulations by an observed magnetogram for the vertical magnetic field. For this work, we use line-of-sight magnetic field from the active region AR 11102, observed on the 30th of August with the Helioseismic and Magnetic Imager (HMI; [Schou et al. 2012](#)) onboard of the Solar Dynamics Observatory (SDO), which is the same as used in [Warnecke & Bingert \(2019\)](#). For all the simulation, we use  $256 \times 256 \times 320$  grid points, that the horizontal resolutions in the simulation and observation are the same. This setup have been successfully used to reproduce the emission features of coronal active region (e.g. [Warnecke & Peter 2019](#)).

### 2.1. Injection of magnetic helicity density

As we want to study the influence of magnetic helicity on coronae, we make use of the fact the simulations are driven by the photospheric magnetic field. We can modify this field in such a way that it becomes more helical without changing the vertical magnetic surface flux. This allows us to study the effect of magnetic helicity on the corona in an isolated way. Throughout this paper, when we discuss magnetic helicity, we mean the magnetic helicity density, defined as

$$H_M = \mathbf{A} \cdot \mathbf{B}. \quad (1)$$

One advantage of our model is that we solve the induction equation in terms of  $\mathbf{A}$  instead of  $\mathbf{B}$ , which makes  $H_M$  directly accessible and it can be easily modified.

The observed vertical magnetic field in the photosphere used to drive the simulation is transformed to  $\mathbf{A}$  using, see [Bingert \(2009\)](#),

$$\hat{A}_x = i \frac{k_y}{k^2} \hat{B}_z \quad \text{and} \quad \hat{A}_y = -i \frac{k_x}{k^2} \hat{B}_z, \quad (2)$$

where the hats indicate the Fourier transform of the quantity,  $k_x, k_y$  are the horizontal and  $k$  the vertical wavenumber with  $k^2 = k_x^2 + k_y^2$ .  $A_z$  is related to the horizontal magnetic field and is normally not prescribed and can evolve freely. We can now use  $A_z$  to include magnetic helicity in the photospheric magnetic field. For this, we set

$$A_z = \frac{H_M^{\text{in}}}{\langle B_z^2 \rangle_{xy}} B_z, \quad (3)$$

where  $\langle \cdot \rangle_{xy}$  indicates horizontal averaging.  $H_M^{\text{in}}$  is our input parameter for controlling the helicity injection. If we multiply

<sup>1</sup> <https://github.com/pencil-code/>

**Table 1.** Summary of runs.

Run	$H_M^{\text{in}}$ [G <sup>2</sup> Mm]	$H_M^{\text{bot}}$ [G <sup>2</sup> Mm]	$E_{H_M^{\text{bot}}}$ [G <sup>2</sup> Mm]	$H_{M \text{ rms}}^{\text{bot}}$ [G <sup>2</sup> Mm]
R	0	$1.3 \times 10^3$	$1.5 \times 10^3$	$2.4 \times 10^3$
M0	0	$2.1 \times 10^3$	$2.9 \times 10^3$	$4.7 \times 10^3$
M3e3	$3 \times 10^3$	$3.7 \times 10^3$	$1.4 \times 10^3$	$5.3 \times 10^3$
M1e4	$1 \times 10^4$	$1.6 \times 10^4$	$1.1 \times 10^3$	$1.6 \times 10^4$
M3e4	$3 \times 10^4$	$4.6 \times 10^4$	$1.6 \times 10^3$	$4.6 \times 10^4$
M1e5	$1 \times 10^5$	$1.5 \times 10^5$	$2.5 \times 10^3$	$1.6 \times 10^5$
M3e5	$3 \times 10^5$	$4.7 \times 10^5$	$8.5 \times 10^3$	$4.7 \times 10^5$
M5e5	$5 \times 10^5$	$7.7 \times 10^5$	$1.6 \times 10^4$	$7.8 \times 10^5$
M1e6	$1 \times 10^6$	$1.4 \times 10^6$	$4.0 \times 10^4$	$1.4 \times 10^6$
M-3e5	$-3 \times 10^3$	$-4.7 \times 10^3$	$9.1 \times 10^3$	$4.7 \times 10^3$

**Notes.**  $H_M^{\text{in}}$  in the injected magnetic helicity density, the only varying input parameter, see Equation (3).  $H_M^{\text{bot}}$  is the horizontal averaged magnetic helicity at the bottom boundary, the photosphere ( $z = 0$ ) with its error  $E_{H_M^{\text{bot}}}$  determined by the time variations.  $H_{M \text{ rms}}^{\text{bot}} = \langle H_M^2(z = 0) \rangle_{xy}^{1/2}$  is the horizontal averaged rms value of the magnetic helicity at the bottom boundary. All values are averaged over the entire simulation times.

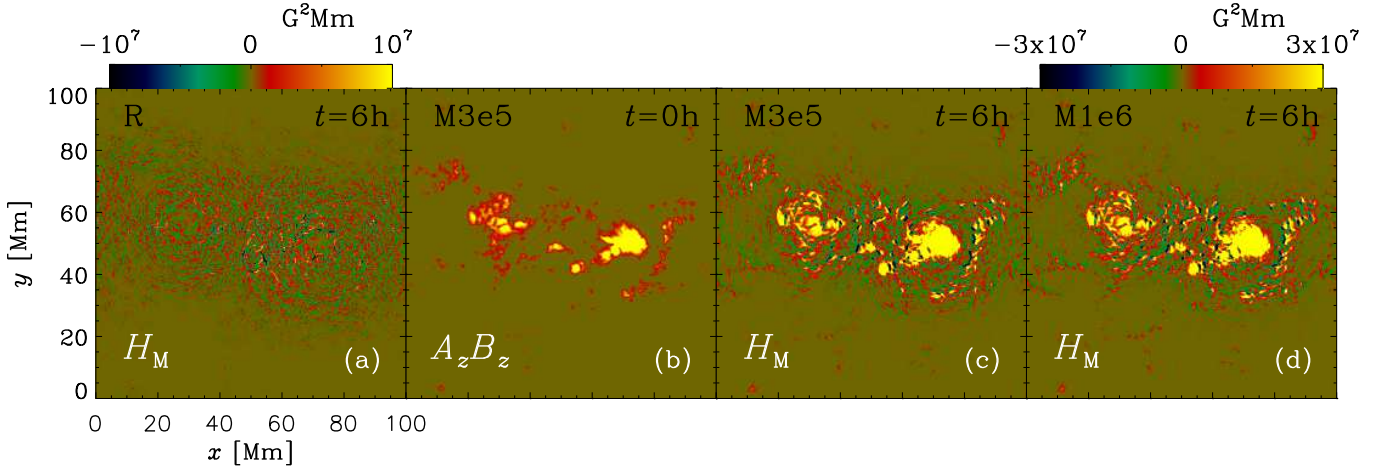


**Fig. 1.** Magnetic helicity distribution at the photosphere for Runs R, M3e5 and M1e6. Panel a shows magnetic helicity  $H_M$  for Run R after 6 hours running time, where no additional helicity is injected. Panel b and c show for Run M3e5 the injected helicity at  $t = 0$  and the helicity after 6 hours running time, respectively. Panel d shows the same as panel c but for Run M1e6. The color table ranges are the same for panels a-c, see Section 3.1.

with  $B_z$  and apply horizontal averaging on both sides we find that the parameter  $H_M^{\text{in}}$  is directly related to the averaged injected magnetic helicity

$$\langle A_z B_z \rangle_{xy} = H_M^{\text{in}}. \quad (4)$$

However, the setting of  $A_z$  also introduces horizontal magnetic fields, which then can contribute to magnetic helicity density via  $A_x B_x$  and  $A_y B_y$ . Therefore, we also define horizontal averaged magnetic helicity at the bottom boundary.

$$H_M^{\text{bot}} = \langle H_M(z = 0) \rangle_{xy} = \langle \mathbf{A} \cdot \mathbf{B} \rangle_{xy}(z = 0), \quad (5)$$

which can be slightly different from the input parameter  $H_M^{\text{in}}$  as discussed in Section 3.1. In the following, we use various values of  $H_M^{\text{in}}$  to drive the corona and investigate their effect on the X-ray production.

## 2.2. Magnetic helicity and its gauge

Before present the results of the numerical simulations, we want to discuss the issues of the gauge dependency of magnetic helicity

in our model. We set the gauge to be the resistive gauge, this means for  $\mathbf{A} \rightarrow \mathbf{A} + \nabla\phi$ , we chose  $\phi = \eta \nabla \cdot \mathbf{A}$ . Hence, if we calculate the magnetic helicity in our simulation it is well defined and consistent among all our simulations. In particular, as we are mostly interested in the scaling of magnetic helicity to X-ray emission, the gauge will not affect our results. Furthermore, the work of Bourdin et al. (2018) have shown that calculating magnetic helicity density using the resistive gauge, the magnetic helicity spectrum and the relative helicity by Berger & Field (1984) give consistent results for a simulation of the solar corona, very similar to the ones used in our work. We are therefore convinced that calculation of magnetic helicity in our gauge is meaningful and we can use the observed values of magnetic helicity (Zhang et al. 2014, 2016) as an motivation to our photospheric helicity injection.

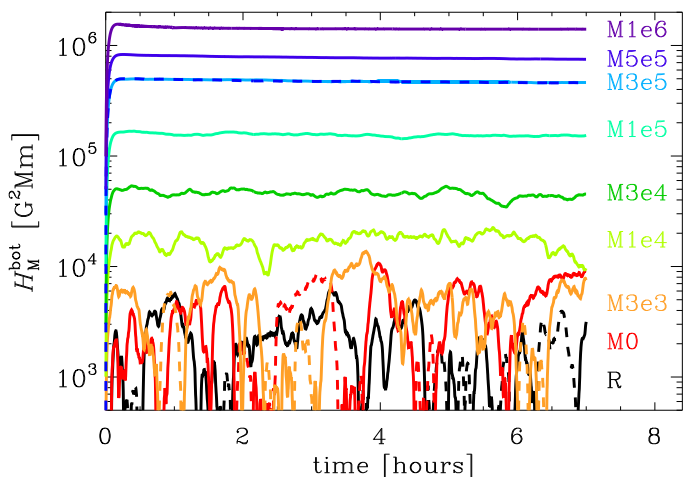


**Fig. 2.** Horizontal averaged magnetic helicity at the photosphere ( $z = 0$ )  $H_M^{\text{bot}}$  as a function of time for all runs. Solid lines show positive values, dashed ones show negative values. The different runs are distinguished by color as indicate by their run name on the right side. We note that Run M-3e5 falls on top Run M3e5 with a negative magnetic helicity as indicated by the dashed line. See Section 3.1.

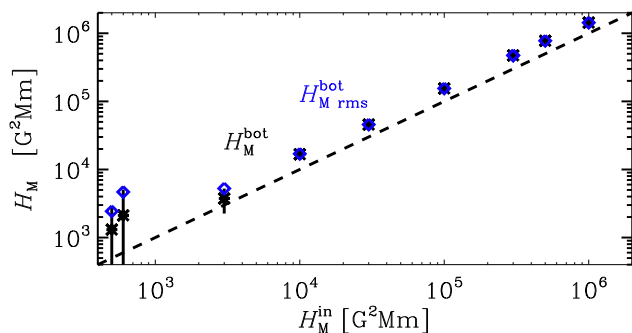


**Fig. 3.** Magnetic helicity at the photosphere  $H_M$  as a function of injected magnetic helicity  $H_M^{\text{in}}$ . The black squares show horizontal averaged values and the blue asterisks show the rms values  $H_M^{\text{bot}}_{\text{rms}}$  at the photosphere ( $z = 0$ ), see Table 1 for exact values. The dashed black line indicate a one-to-one relation. Runs R and M0 have been moved to  $H_M^{\text{in}} = 0.05$  and  $0.06$   $\text{G}^2\text{Mm}$ , respectively, to be able to include these runs in the plot, even though their values are zero. All values are averaged in time over entire running time. See Section 3.1.

### 3. Results

For our work we use ten runs where we increase the magnetic helicity injected in the photosphere. Run R is the reference run, where  $A_z$  in the photosphere is not modified, hence no helicity injected. This run is similar to Run Ba of [Warnecke & Bingert \(2019\)](#). In all other runs we set  $A_z$  according to Equation (3). The number after 'M' in the run names indicates the value of injected magnetic helicity in  $\text{G}^2\text{Mm}$ , see Table 1. Run M0 no magnetic helicity is injected, however, because  $A_z$  is set to zero in the photosphere, the run is different from Run R, where  $A_z$  can freely evolve. One run has been injected with a negative magnetic helicity to check whether or not the sign is important for the amount of X-ray emission. We chose the values of magnetic helicity motivated by the measurements of [Zhang et al. \(2014, 2016\)](#), where typical active region have values from  $10^4$  up to  $5 \times 10^5$   $\text{G}^2\text{Mm}$ .

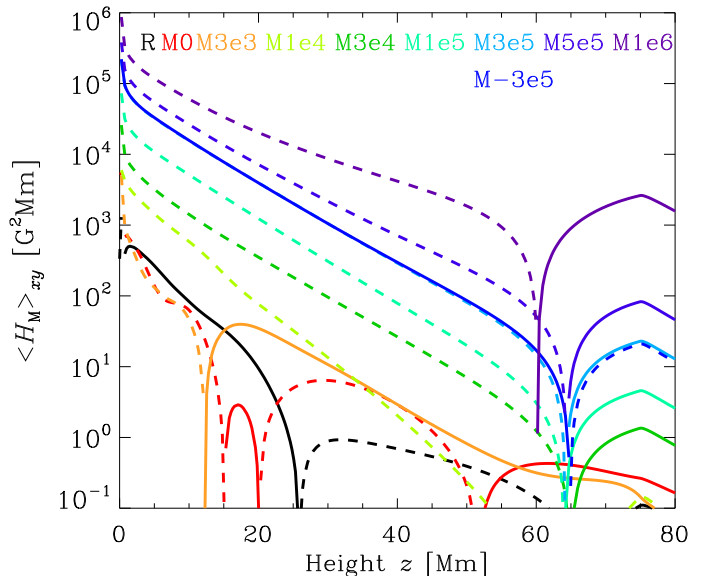


**Fig. 4.** Horizontal averaged magnetic helicity at a function of height  $z$  for all runs. As in Fig. 2, solid lines indicate positive values, dashed indicate negative values. The colors indicate the different runs. All values are averaged in time over the relax stage of the runs. See Section 3.1.

All the runs have run seven hours to be well in a relaxed stage, in which the averaged temperature, ohmic heating and X-ray emission do not change significantly in time. As is common for such kind of simulations, the initial phase is dominated by building up a self-heated corona independent on the initial temperature and density profiles. This is mostly set by the radiative cooling time in these models. For our further analysis we use the time after 4.6 hours as a relaxed stage and calculate most of our results from this stage.

#### 3.1. Helicity evolution and distribution

First we present the distribution of magnetic helicity injected in the photosphere. If magnetic helicity is not prescribed via Equation (3), it is initially zero. However, because of the photospheric motions interacting with the photospheric magnetic field, magnetic helicity is generated, as shown in Fig. 1a for Run R. The helicity is distributed around the two magnetic polarities of the active region showing both sign of helicity varying around the zero level. The horizontal averaged value is small and varies over time between positive and negative values (Fig. 2). These values are consistent with calculated ones of [Bourdin et al. \(2018\)](#) for their simulation of the solar corona. The time average is small with an error larger than the value, see third and forth row of Table 1. The error is estimated by the largest difference between the mean of each third of the time series. This means that at each time there a non-zero magnetic helicity present in the photosphere, however the time average does not lead to preferred sign. Run M0 behaves similarly but with a higher time averaged value and a larger error.

For the other runs, where we inject helicity, the actual helicity in the photosphere is the sum of the injected and the by photospheric motions generated helicity. This can be seen in Fig. 1 for Run M3e5. In Panel b, we show the injected helicity at beginning of the simulation  $t = 0$ , when the photospheric motions are zero. There, the helicity is proportional to  $B_z^2$  as given by Equation (3) and has peak value of  $\pm 10^7$   $\text{G}^2\text{Mm}$ . This distribu-

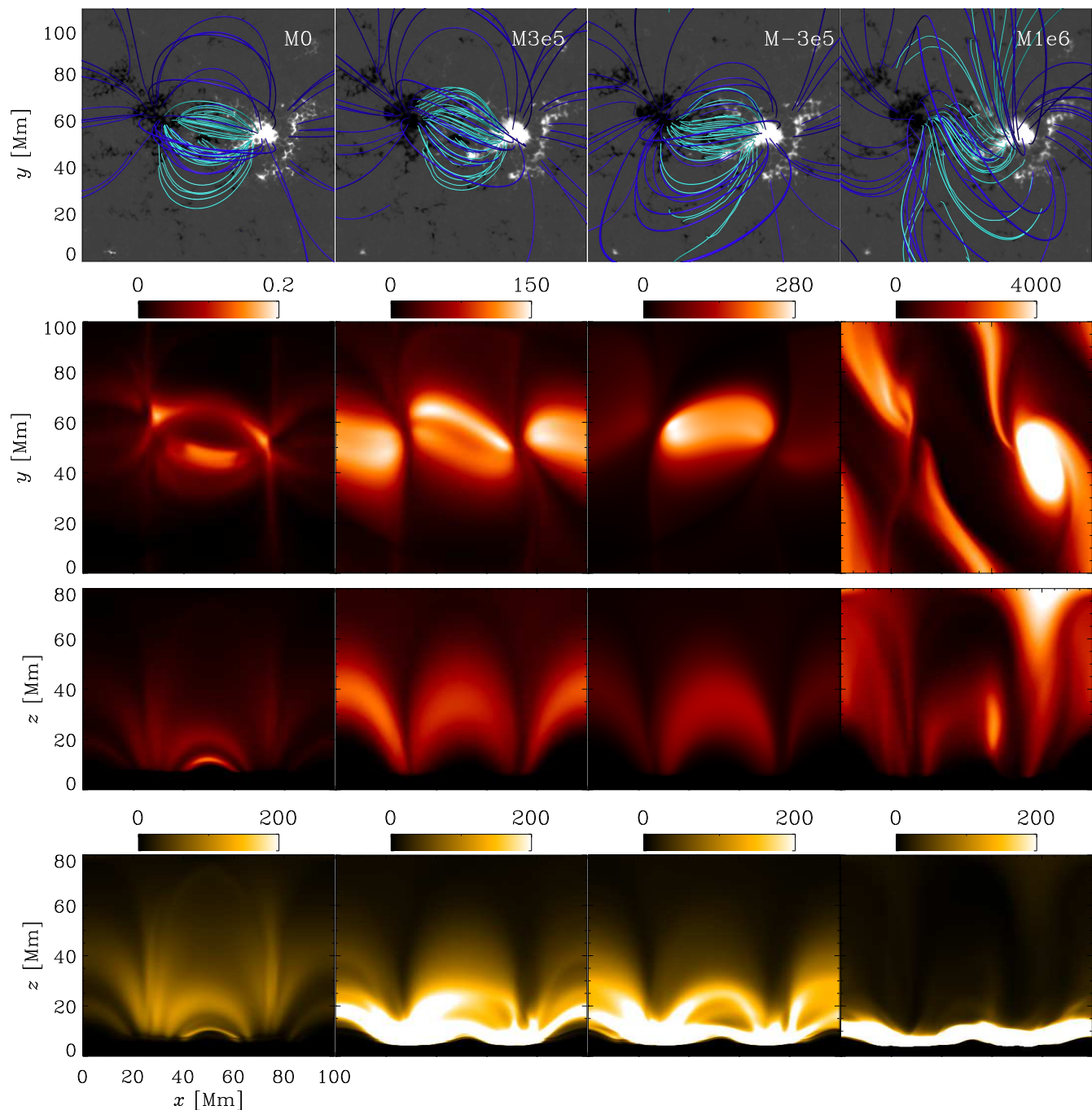


**Fig. 5.** Magnetic field lines configuration and X-ray and EUV emission for Runs M0, M3e5, M-3e5 and M1e6. The first row shows the vertical magnetic field at the photosphere (white outward, black inwards, between  $-100$  and  $100$  G) together with traced magnetic field lines. The light blue lines show the close connecting magnetic field between the two polarities and the dark blue shows the larger arching fields connecting the two. The region of the seeds for the field line tracing are the same for each runs. The second and third row show the synthesized X-ray emission using the Hinode/XRT Al-poly temperature response function as top view ( $xy$ ) and side view ( $xz$ ), respectively. The last row shows the synthesized EUV emission using the temperature response function for the AIA  $171 \text{ \AA}$  channel. The plots have been calculated from a six-hour snapshot of each simulation. The emissions are plotted in units of  $\text{DN pixel}^{-1}$ . See Section 3.2.

tion mimic the actual distribution of helicity in active region well (Zhang et al. 2014, 2016). In the relax stage, see Fig. 1c, the by photospheric motions generated helicity is added to the injected helicity. As shown in Fig. 1c for runs with even higher magnetic helicity, the structure does not change, only the amplitudes become stronger. Furthermore, the injected helicity via  $A_z$  also enhances the horizontal magnetic field, which lead to additional

contribution via  $A_x B_x$  and  $A_y B_y$ . Hence, the time averaged values are always around 1.5 times higher than the injected helicity values, see Table 1 and Fig. 3. Only for runs with low magnetic helicity (Runs R to M3e3) the time variations are comparable to the mean value, see Fig. 2 and therefore the rms value is different from the mean value, see Fig. 3 and Table 1. As the mean value and the rms (for most of the runs) is proportional to the injected

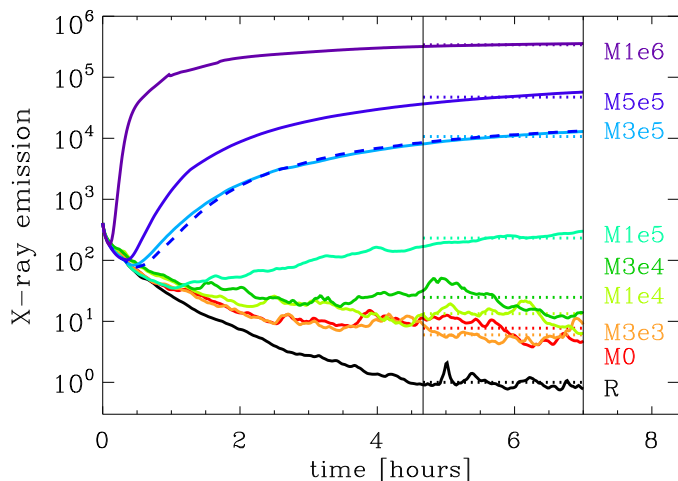


**Fig. 6.** Time series of the total synthesized X-ray emission for all runs. The emission is normalized by the one of Run R in the relax stage. The dashed purple line shows Run M-3e5. The solid vertical line indicate the beginning of the relax stage (after 4.7 hours). See Section 3.2.

value, we can use the injected magnetic helicity as a reasonable input parameter describing the helicity in the photosphere well.

Next we look at the height distribution of magnetic helicity in our simulations. Interestingly for all of the runs, the magnetic helicity has a different sign in the corona than in the photosphere, see Fig. 4. If we inject positive helicity, we find negative helicity just above the first grid layers. This is mostly likely an artifact of how the magnetic field in terms of the vector potential is set at the boundary. We find this behavior also in Run R, so it is not an artifact of the helicity injection. Furthermore, the absolute value of helicity shows a smooth decrease in the grid layers near the boundary. The actual sign of helicity do not matter for our study as it become clear in the analysis below.

For most of the runs helicity decreases exponentially with a similar scaling height of around 6-7 Mm. This is similar to the scaling height of ohmic heating in these kind of simulations (e.g. Gudiksen & Nordlund 2005; Bingert & Peter 2011). For runs with low injected helicity (Runs R to M1e4) the sign of averaged helicity changes multiple times in the corona showing no distinct pattern. For larger injected helicities (Runs M3e5 to M1e6), we find only one reversal occurring for all runs around 65 Mm. This might be because of the limited size of the domain. We do not find any correspondence between location where the sign of magnetic helicity changes and the location of plasma  $\beta = 1$  as found by Bourdin et al. (2018). We think that this is a special property of their simulation and not a general feature. However, the fact that the sign changes in the corona of our simulations agrees well with the observational result that magnetic helicity has the opposite sign in the heliosphere than on the solar surface (Brandenburg et al. 2011), which have been also found in helical dynamo simulations with coronal envelope (Warnecke et al. 2011, 2012) and in solution of simple dynamos with a force-free corona (Bonanno 2016).

### 3.2. Magnetic field and emission structure

The injection of magnetic helicity at the photosphere affects the magnetic field structure in the corona of each simulations. As shown in the top row of Fig. 5, the vertical magnetic field in the photosphere do not change, if magnetic helicity is injected.

However, field line topology visible as a field line twist undergoes significant changes due to various levels of magnetic helicity in the photosphere. For Run M0 (and similar for Run R), the magnetic field lines show potential-like arch structures. Increasing magnetic helicity let the field lines be become more helical forming sigmoid-like shapes. For the largest helicity input (Run M1e6), the field lines are forming large complex arcs instead on small close connecting arcs, which are most pronounced in the light blue field lines, see first row of Fig. 5. We note here that due to the periodic boundary condition the field lines can connect through the horizontal boundary. As expected, an opposite sign of helicity forms a sigmoid with the opposite handiness. Except the handiness, the arc structures does not depend on the sign of magnetic helicity, as the magnetic field line topology of Run M-3e5 is a mirror image of the ones of Run M3e5. The small differences can be mostly associated to the field line tracing algorithm and the non-symmetry of the active regions.

The main goal of this work is to relate the X-ray emission to the injected magnetic helicity. For this we synthesis the X-ray emission as it would be observed with the X-ray Telescope (XRT; Golub et al. 2007) on the HINODE spacecraft (Kosugi et al. 2007) using the Al-poly channel. We use the density and temperature of the model to calculate the emission using the temperature response function calculated with the help of CHIANTI database (Dere et al. 1997; Del Zanna et al. 2015). This emission calculation assumes an optical thin solar corona and is either integrated in the  $z$  or  $y$  direction to mimic a line-of-sight and a side view, respectively. We find magnetic helicity affects strongly the X-ray emission. As shown in the second and third row of Fig. 5 for the top ( $xy$ ) and the side ( $xz$ ) view of the synthesis X-ray emission larger helicity input lead to higher X-ray emission. For no magnetic helicity input the X-ray emission is very weak and a result of a low temperature corona with a potential-like field structure. For higher magnetic helicity the X-ray emission becomes significantly stronger and also the loop structure changes. For Run M0 the weak emission comes from small low connecting loop, but is so weak that the XRT would never able to detect it. For Runs M3e5 and M3e-5, the X-ray emission show twisted sigmoid-like loop structures, aligned with the magnetic field topology seen in the row above. For the high magnetic helicity case of Run M1e6 the X-ray emission reveals highly twisted loops structures, which are significantly deformed by the twist of the magnetic field. The twist is even so strong that it causes the magnetic field to interact with the upper boundary and forms a locally enhanced ohmic heating region, which produce strong X-ray emission. Even though this emission region is an artifact, its effect on the averaged total emission is comparable to the temporal variation inside the relaxed stage and therefore do not affect our results of X-ray emission scaling below. Already from these plot we find that the X-ray emission increases larger than linear for increasing magnetic helicity.

The extreme UV emission is also affected by the injection of magnetic helicity. We focus on the bands in extreme UV emission as they would be observed by the Atmospheric Imaging Assembly (AIA; Lemen et al. 2012). Similar as for the X-ray emission calculation we use the temperature and density in each simulation together with temperature response kernel (Boerner et al. 2012)<sup>2</sup> of several AIA channels. As an example we show in the last row of Fig. 5 the emission of the AIA 171 Å channel. Runs with higher magnetic helicity show not only more emission, but also with a different structure. For Runs M3e5 and

<sup>2</sup> Implemented in SolarSoft (<http://www.lmsal.com/solarsoft/>).

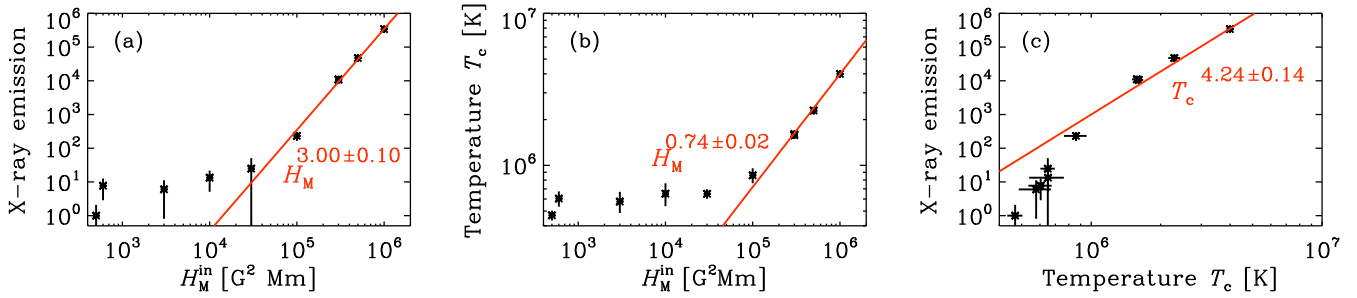


**Fig. 7.** Scaling of X-ray emission with magnetic helicity and coronal temperature. We show the total X-ray emission over injected magnetic helicity  $H_M^{\text{in}}$  (a), coronal temperature  $T_c$  over  $H_M^{\text{in}}$  (b) and X-ray emission over coronal temperature  $T_c$  (c). The red line is a power-law fit over the last five data points with corresponding slope in red. The X-ray emission is time-averaged over the relaxed stage (4.6 to 7 hours) and normalized by total emission of Run R. The coronal temperature is averaged in horizontal directions, in height ( $z=18$  to  $20$  Mm) and over the relaxed stage. The errors are estimate from the time variation in the relaxed stage. As in Fig. 3 we moved Runs R and M0 to  $H_M^{\text{in}}=0.05$  and  $0.06$   $\text{G}^2\text{Mm}$ , respectively, to include them in the plot. See Section 3.3.

M3e-5, the emission comes from coronal loops structures which also radiates in the X-ray band, however the EUV seems to be slightly at lower heights than the X-ray emission. In contrast, for Run M1e6, the EUV complete vanish from the coronal loops structures and emits only from the coronal base at around  $z=10$  Mm. We discuss this issue in more detail, when we compare the scaling of total emission of EUV and X-ray emission with helicity, see Section 3.4.

As our analysis is focused on the X-ray emission, we use this emission to determine the relaxed stage of our simulations. For this we plot in Fig. 6 the time evolution of the total X-ray flux, integrated over the entire simulation domain. For all the runs the total X-ray emission becomes quasi-steady in time after around 4.6 hours. We define the quasi-steady stage as a stage when the temporal variation are small compare to the average. We call this time interval the relaxed stage and apply all the time averages over it, which are used in the analysis below. The duration of the initial phase is determine by the cooling time in system. As the Run R has a very low temperature corona the cooling times is therefore much longer than for the other runs, as seen also in the X-ray emission. Already in this plots we also see an indication of a power-law relation with an index larger than one between the X-ray emission and the injected magnetic helicity.

### 3.3. Scaling of X-ray emission

Now we turn to question how total integrated X-ray emission depends on the injected magnetic helicity. As shown in in Fig. 7a, we find a clear increase of X-ray emission for larger injected helicity. For runs with helicities starting with  $3e5$   $\text{G}^2\text{Mm}$  we find a power-law relation with a slope of 3. For lower helicities the increase is much lower. This indicates that the helicity has to overcome a threshold of around  $3e5$   $\text{G}^2\text{Mm}$  before influencing the X-ray emission significantly. This relation is tightly connected to the increase of coronal temperature  $T_c$  with injected helicity as shown in Fig. 7b. There we find that the coronal temperature increase with helicity with a power-law exponent of 0.74. for the runs with higher helicity. The temperature is averaged in horizontal directions, in height ( $z=18$  to  $20$  Mm) and over the relaxed stage to describe a typical coronal temperature of each simulation. Also here a threshold of around  $3e5$   $\text{G}^2\text{Mm}$  is present. The power law relation of X-ray emission and temperature of  $T_c^{4.24 \pm 0.14}$  follows closely the relation obtained from stars  $T_c^{4.5 \pm 0.3}$  (Güdel 2004) and is close the relation of  $T^4$  expected from thermal black body radiation. However, we should keep in

mind that also the density enters the calculation of X-ray emission. Hence, the part of the increase of X-ray emission is also due to the increase of density inside the emitting X-ray loops. Getting a consistent temperature X-ray relation make us confident we can use our results to understand the stellar X-ray emission as a function of helical magnetic fields.

Before discussion the implication of this result for stellar activity we investigate why magnetic helicity actually increases the X-ray emission in the way as we found in our simulations. First of all, as discussed above the X-ray can be directly related to the coronal temperature either by using the observed relation or even a simple black boundary radiator, where the emission is proportional to the temperature to forth power. Our runs with high magnetic helicity are well in agreement with these two relations. The coronal temperatures in all simulations can be directly related to vertical Poynting flux into the corona, as the energy flux going into the corona must be the same as the energy flux going out of the corona. The higher the Poynting flux, the higher the coronal temperature. The Poynting flux in our simulation is given

$$\mathbf{S} = \eta \mathbf{J} \times \mathbf{B} - \frac{1}{\mu_0} (\mathbf{u} \times \mathbf{B}) \times \mathbf{B}, \quad (6)$$

where the first term is only important in the few lowest grid layers. In Fig. 8a we show the vertical Poynting flux  $S_z$  at the height, where plasma  $\beta$  is around unity, over magnetic helicity. Plasma  $\beta$  is defined as the ration of gas and magnetic pressure and normally indicated the dominance of magnetic (thermal) energy as low (high) values. We chose this height, because there the flow field can still dominate the magnetic field evolution and the Poynting flux give a good indication for the energy flux into the corona. The vertical Poynting flux increases with injected helicity for last four runs with power-law relation of around 1.8. For runs with low helicity the Poynting flux is not or only weakly increasing helicity. This results in a relation of X-ray emission to Poynting flux with a slope of around 1.8 for runs with high helicity and an inconclusive relation for runs with low helicity, see Fig. 8b. However, the coronal temperature is can be related to the Poynting flux with a power-law including all runs, meaning this relation is general and not dependent on helicity. Hence, the reason why the runs with lower helicity do not show a strong increase of coronal temperature with helicity must be due to the relation of helicity to Poynting flux. The Poynting flux in our simulation consists mostly of the horizontal motions interacting with the horizontal and vertical magnetic field. The vertical magnetic field and the horizontal motions are the same for all simu-

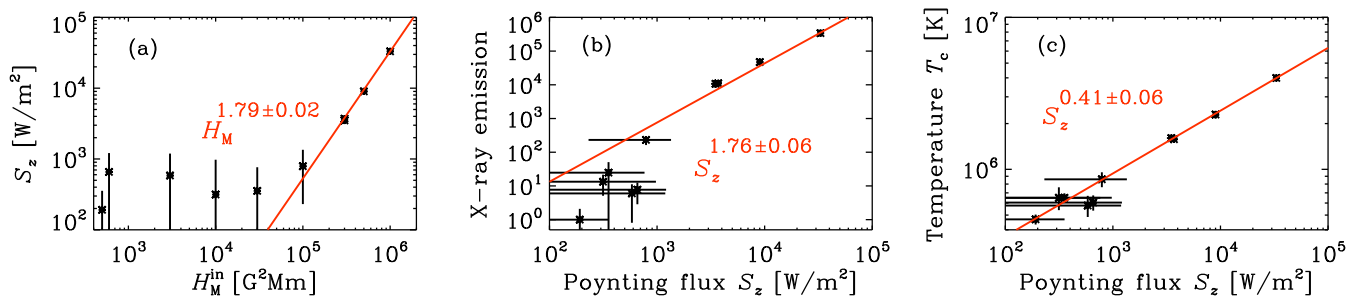


**Fig. 8.** Scaling of Poynting flux with magnetic helicity, X-ray emission and coronal temperature. We show the vertical Poynting flux  $S_z$  over injected magnetic helicity  $H_M^{\text{in}}$  (a), X-ray emission over vertical Poynting flux  $S_z$  (b) and coronal temperature  $T_c$  over vertical Poynting flux  $S_z$  (c). The red line is a power-law fit over the last five data points with a corresponding slope in red. The vertical Poynting flux is calculated in the region, where plasma  $\beta$  is close to unity ( $z = 3 - 4$  Mm) and averaged horizontally and over the relaxed stage. Otherwise the same as Fig. 7. See Section 3.3.

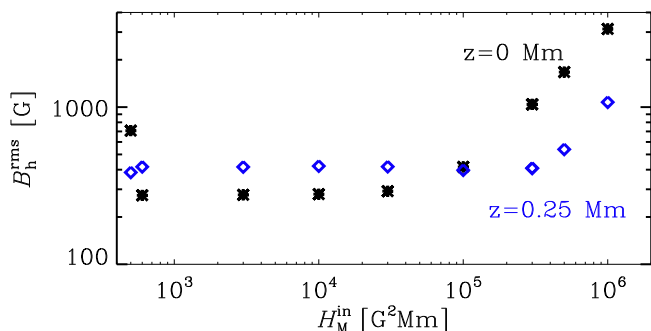


**Fig. 9.** Horizontal magnetic field  $B_h^{\text{rms}}$  near the photosphere and injected magnetic helicity  $H_M^{\text{in}}$ . We plot rms values of the horizontal magnetic field at  $z = 0$  (black asterisks) and  $z = 0.25$  Mm (blue diamonds) over  $H_M^{\text{in}}$ . We moved Runs R and M0 to  $H_M^{\text{in}}=0.05$  and  $0.06$   $\text{G}^2\text{Mm}$ , respectively, to include them in the plot. See Section 3.3.

lations, because they are prescribed at the photospheric boundary. Therefore, the magnetic helicity changes the Poynting flux via the horizontal magnetic field. As plotted in Fig. 9, the root mean squared of the horizontal magnetic field  $B_h^{\text{rms}}$  near the photosphere changes only above the threshold of  $3e5$   $\text{G}^2\text{Mm}$ . The discrepancy between the height, where the Poynting flux and the horizontal magnetic field is calculated are not significant. The Poynting flux near the photosphere follow a similar behavior as at  $z = 3 - 4$  Mm, where plasma  $\beta$  is unity; there, the values of the time-averaged Poynting flux are close to zero or even negative, therefore the scaling relation as shown in Fig. 8a is not possible to determine. Runs R and M0 have also different values of horizontal magnetic fields, because  $A_z$  in the photosphere is set to zero in Run M0 but not set in Run R, see Fig. 8a and Section 3.1. This might also explain their different X-ray emission and coronal temperatures for similar values of photospheric helicity. To conclude, adding magnetic helicity to a photospheric magnetic field has only a significant effect, if the resulting horizontal magnetic field exceeds the exiting horizontal field.

The fact that X-ray emission is sensitive to the amount of magnetic helicity at the photosphere can have a large impact on stellar activity. Magnetic helicity related to active region is thought to be produced by the underlying dynamo. Using mean-field theory, the  $\alpha$  effect produces both sign of magnetic helicity, one sign of large scales, the other on small scales. (Brandenburg & Subramanian 2005). The large scales in this context means the scale of the whole stars, small scales everything significantly

below. Hence, magnetic field from active region is counted as a small scale field in this view. However, as the sign for the results of our work is not important, for our estimate it does not matter, if the magnetic helicity injected in our simulation is produced at large or small scales. The amount of helicity produced on both scales is  $2\alpha\bar{B}$  (Krause & Rädler 1980), where  $\bar{B}$  is the large scale field. The  $\alpha$  is proportional to the rotational influence of the Star as it is proportional to the kinetic helicity (Steenbeck et al. 1966). However, recent measurement from global convective dynamo simulations indicate that  $\alpha$  has a more complicated distribution and a different values than the theoretical expression invoking the kinetic helicity (Warnecke et al. 2018; Viviani et al. 2019). Furthermore, recent studies found a scaling of the  $\alpha$  effect with rotational influence to the power of around 0.7 (Warnecke 2018) or 0.5 (Warnecke & Käpylä 2019). If we now use this scaling of magnetic helicity with rotational influence together with our scaling of X-ray emission with magnetic helicity, we get that the X-ray emission scales with the power of around 3 using the theoretical scaling of  $\alpha$  or around 2 to 1.5 using the  $\alpha$  effect measurements. All values predict are large impact of the magnetic helicity in the relation of X-ray emission and rotation of stars. Increasing the magnetic helicity alone without the magnetic flux is enough to reproduce a scaling similar or even larger what is found by stellar observation studies (e.g. Pizzolato et al. 2003; Vidotto et al. 2014; Reiners et al. 2014; Wright & Drake 2016), in which the scaling is around 2.

### 3.4. Relation to extreme UV emission

Beside the X-ray emission we investigate how the extreme UV emission depends on the magnetic helicity. EUV emission cannot be observed from other stars than the Sun, however we can use these emission measures to probe the atmospheric properties for different kind of stellar activity levels. For this we synthesized the main AIA coronal channels as described in Section 3.2 and plot them as function of injected magnetic helicity in Fig. 10a. All EUV emissions show an increase with higher injected helicity. Their slopes determined from the last five highest helicities are weaker than the increase of X-rays as shown in Fig. 7a. The slopes show a clear temperature dependence. For high temperatures emission as in the 94 and 211 Å channels the increase goes with the power of around 1.5, this slope decreases for temperatures around 1 MK (171 Å channel) and then increases again for temperatures of around 200.000 K (304 Å channel). This show each channel has a significant different magnetic helicity sensitivity. As seen in the scaling of X-ray emis-



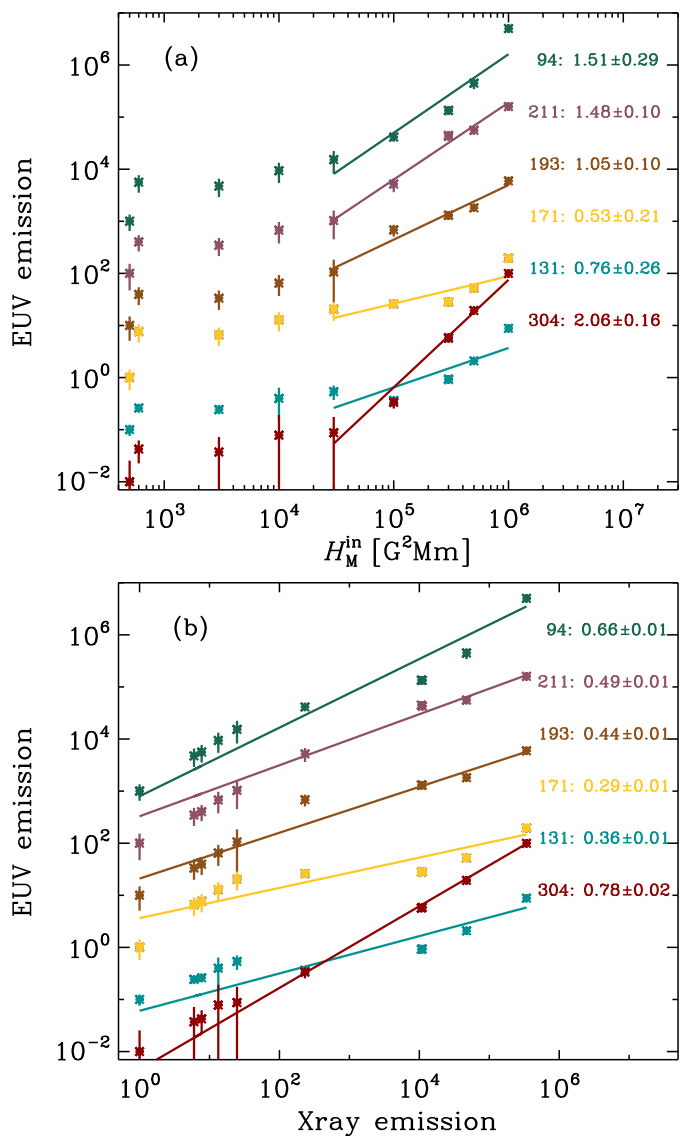


**Fig. 10.** EUV emission as a function of injected magnetic helicity  $H_M^{\text{in}}$  (a) and X-ray emission (b). Total EUV emissions of the AIA channels 94, 211, 193, 171, 131, 304 Å are indicated by their corresponding wavelength in Å and color. We fit a power-law fit to the last five points (a) or all points (b) and give the slopes next to their channel number. All points have been normalized to the emission of Run R and then shifted to get a factor of ten ration between the set of points for each emission to increase visibility. We have ordered the emission based on their peak temperature with the highest on the top. We moved Runs R and M0 to  $H_M^{\text{in}}=0.05$  and  $0.06$  G<sup>2</sup>Mm, respectively, to include them in panel a.

sion, temperature and Poynting with magnetic helicity, only the five highest magnetic helicity cases show a clear power-law behavior. This behavior can be partly explained by the different temperature response function of each emission channel. Additionally, the temperature does also effect the density distribution in each simulation making coronal loop denser for higher temperatures and less dense for lower temperature. This will than also effect the synthesis emission calculations. From measurements of emission from the Sun and other stars, it is found that the emission from higher temperatures are more sensitive to the surface magnetic field. (e.g. Schrijver et al. 1989; Barczynski et al. 2018). This seems to be also true for the sensitivity of mag-

netic helicity. However, the difference is that the 304 Å channel is more sensitive than the slightly higher temperature. This could be an artifact, as at the temperatures and heights, where this emission is radiated, the atmosphere is not fully optical thin any more.

Of further interest is the relation between different emission channels, the is often called a flux-flux relation referring to the relation of different emission fluxes (e.g. Schrijver 1987). In Fig. 10b we relate the X-ray emission to several EUV channels. Interestingly, we find power-law relations, which fits all runs and not just to the ones with highest magnetic helicity. This again means, that the general emission properties are similar in each of the simulation and just the relation between magnetic helicity and Poynting flux. One can also say that the horizontal magnetic field is the quantity, which causes the difference between the low helicity runs and the high helicity runs. Also in the relation between X-ray emission and EUV emission we find that the slope depends strongly with temperature. At the high and low temperature ends, we have larger slopes and weaker ones for around 1MK. As a consequence, the relation of Fig. 10 indicate that the magnetic helicity is more sensitive to X-ray emission rather than EUV emission. Hence, magnetic helicity related phenomena can be easier traced with X-ray emission than with other EUV emission channels. To compare one of the channels with stellar observation we can use the 304 Å channel, which probe emission from the chromosphere and transition as a proxy for the CI v emission, routinely measure for other stars. Schrijver (1987) find that the X-ray flux depend on CI v with a power of 1.5, which is reasonable close to  $1/0.78 = 1.28$  of our findings. However, more recent measurement of chromospheric Ca II H&K emission and its dependence on X-ray flux gives a power law of 0.4 (Mittag et al. 2018), which is closer to our scaling of the emission in the 131 and 171 Å channel than the 304 Å channel.

Another aspect in the comparison of X-ray emission and EUV emission is the their location of emission. As shown in Fig. 5, the X-ray emission is emitted from the coronal loop structures for medium and large helicities, the EUV on the other hand is emitted from the coronal loops only at the medium helicities. Interestingly if one compares the decrease of emission with height for these different runs, see Fig. A.1, one finds that the emission falls off with a similar scale height for moderated helicities. However, for large helicities the emission is strongly concentrated in the low corona. This is in contradiction to the emission signatures found in solar active regions with high activity. Even though there also the X-ray emission reaches high values and form loops structures similar in our simulations, the EUV emission is still visible in large part of the corona and forming also loops. This point into the direction that the Sun do not form very active regions in the same process as discussed here, however, the active region driving our simulations in the photosphere is also a very simple one, in contrast to strong active regions on the Sun, which are often very complex.

## 4. Conclusions

For the first time, we have used numerical 3D MHD simulations of the solar corona to study the effect of magnetic helicity on the coronal properties in particular the coronal X-ray emission. We found that for higher injected magnetic helicity at the photosphere the corona becomes hotter and emits significantly more X-ray emission. We determine that the X-ray emission increases with cubically with the injected helicity. Using this scaling with the typical scaling of magnetic helicity on rotation, we find that

can explain the increase of stellar X-ray luminosity with rotation alone by the increase of magnetic helicity with rotation. Therefore with this work we can show that the magnetic helicity can have a larger impact on the rotation-activity relation of stars.

The increase of magnetic helicity increases the horizontal magnetic field in the photosphere and therefore the photospheric Poynting flux. The higher Poynting flux leads to higher coronal temperatures and larger X-ray flux, following a  $T_{rmc}^{4.24 \pm 0.14}$  relation in agreement with stellar observations (Güdel 2004). Furthermore, we found that the increase of magnetic helicity reproduce the scaling of chromospheric & transition zone emission well as stars predicted.

We find that the reversal of magnetic helicity in the corona is not related to the location, where plasma  $\beta$  is unity, in contrast to the work of Bourdin et al. (2018). However, horizontal averaged helicities show at least one reversal in the corona of each of our simulation and is therefore in agreement with the studies by Brandenburg et al. (2011) and Warnecke et al. (2011, 2012).

Future studies will include the injection of helicity with more complex distribution of values and signs. Furthermore, we will test the difference between the injection of helicity with our method and the injection of helicity flux as used observationally studies (e.g. Chae et al. 2001; Nindos et al. 2003; Maeshiro et al. 2005; Vemareddy 2019).

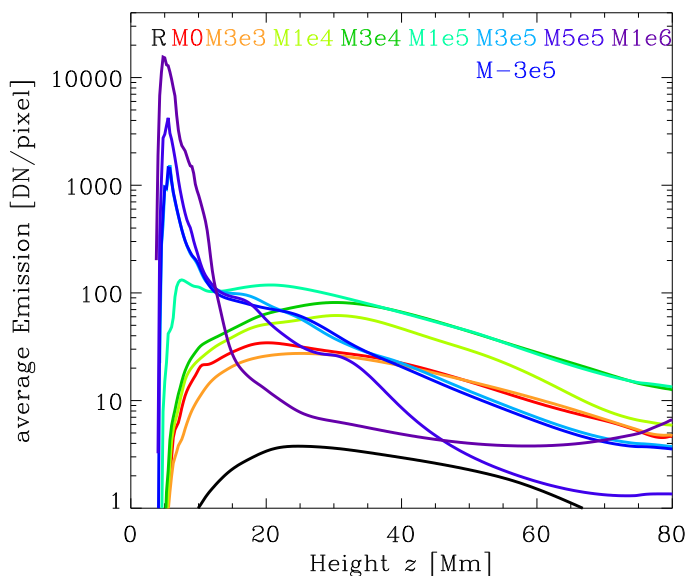


**Fig. A.1.** Height dependency of horizontal averaged emission of the AIA 171 Å channel. The color of the lines indicate the different runs as displayed in the top of the plot.

## Appendix A: Emission over height

To further show, how the UV emission depends on injected helicity, we plot in Fig. A.1, the height dependence of the horizontal averaged UV emission.

*Acknowledgements.* The simulations have been carried out on supercomputers at GWDG, on the Max Planck supercomputer at RZG in Garching and in the facilities hosted by the CSC—IT Center for Science in Espoo, Finland, which are financed by the Finnish ministry of education. J.W. acknowledges funding by the Max-Planck/Princeton Center for Plasma Physics and from the People Programme (Marie Curie Actions) of the European Union’s Seventh Framework Programme (FP7/2007-2013) under REA grant agreement No. 623609.

## References

- Augustson, K. C., Brun, A. S., & Toomre, J. 2019, *ApJ*, 876, 83  
 Barczynski, K., Peter, H., Chitta, L. P., & Solanki, S. K. 2018, *A&A*, 619, A5  
 Berger, M. A. & Field, G. B. 1984, *Journal of Fluid Mechanics*, 147, 133  
 Bingert, S. 2009, PhD thesis, Albert-Ludwig-Universität Freiburg  
 Bingert, S. & Peter, H. 2011, *A&A*, 530, A112  
 Bingert, S. & Peter, H. 2013, *A&A*, 550, A30  
 Boerner, P., Edwards, C., Lemen, J., et al. 2012, *Sol. Phys.*, 275, 41  
 Bonanno, A. 2016, *ApJ*, 833, L22  
 Bourdin, P., Singh, N. K., & Brandenburg, A. 2018, *ApJ*, 869, 2  
 Brandenburg, A. & Subramanian, K. 2005, *Phys. Rep.*, 417, 1  
 Brandenburg, A., Subramanian, K., Balogh, A., & Goldstein, M. L. 2011, *ApJ*, 734, 9  
 Chae, J., Wang, H., Qiu, J., et al. 2001, *ApJ*, 560, 476  
 Chatterjee, P. 2018, *Geophys. Astrophys. Fluid Dyn.*, submitted, arXiv:1806.08166 [arXiv:1806.08166]  
 Del Zanna, G., Dere, K. P., Young, P. R., Landi, E., & Mason, H. E. 2015, *A&A*, 582, A56  
 Dere, K. P., Landi, E., Mason, H. E., Monsignori Fossi, B. C., & Young, P. R. 1997, *A&AS*, 125, 149  
 Golub, L., DeLuca, E., Austin, G., et al. 2007, *Solar Physics*, 243, 63  
 Gombosi, T. I., Tóth, G., De Zeeuw, D. L., et al. 2002, *Journal of Computational Physics*, 177, 176  
 Gosain, S. & Brandenburg, A. 2019, *ApJ*, 882, 80  
 Güdel, M. 2004, *A&A Rev.*, 12, 71  
 Gudiksen, B. V. & Nordlund, Å. 2002, *ApJ*, 572, L113  
 Gudiksen, B. V. & Nordlund, Å. 2005, *ApJ*, 618, 1020  
 Kosugi, T., Matsuzaki, K., Sakao, T., et al. 2007, *Solar Physics*, 243, 3  
 Krause, F. & Rädler, K.-H. 1980, *Mean-field Magnetohydrodynamics and Dynamo Theory* (Oxford: Pergamon Press)

- Lemen, J. R., Title, A. M., Akin, D. J., et al. 2012, *Sol. Phys.*, 275, 17  
 Maeshiro, T., Kusano, K., Yokoyama, T., & Sakurai, T. 2005, *ApJ*, 620, 1069  
 Mittag, M., Schmitt, J. H. M. M., & Schröder, K. P. 2018, *A&A*, 618, A48  
 Moffatt, H. K. 1978, *Magnetic Field Generation in Electrically Conducting Fluids* (Cambridge: Cambridge University Press)  
 Nindos, A., Zhang, J., & Zhang, H. 2003, *ApJ*, 594, 1033  
 Pariat, E., Leake, J. E., Valori, G., et al. 2017, *A&A*, 601, A125  
 Pevtsov, A. A., Fisher, G. H., Acton, L. W., et al. 2003, *ApJ*, 598, 1387  
 Pizzolato, N., Maggio, A., Micela, G., Sciortino, S., & Ventura, P. 2003, *A&A*, 397, 147  
 Reiners, A., Schüssler, M., & Passegger, V. M. 2014, *ApJ*, 794, 144  
 Schou, J., Scherrer, P. H., Bush, R. I., et al. 2012, *Sol. Phys.*, 275, 229  
 Schrijver, C. J. 1987, *A&A*, 172, 111  
 Schrijver, C. J., Cote, J., Zwaan, C., & Saar, S. H. 1989, *ApJ*, 337, 964  
 Schrunner, M., Pettidmange, L., Raynaud, R., & Dormy, E. 2014, *A&A*, 564, A78  
 Singh, N. K., Käpylä, M. J., Brandenburg, A., et al. 2018, *ApJ*, 863, 182  
 Steenbeck, M., Krause, F., & Rädler, K.-H. 1966, *Zeitschrift Naturforschung Teil A*, 21, 369  
 Vemareddy, P. 2019, *ApJ*, 872, 182  
 Vidotto, A. A., Gregory, S. G., Jardine, M., et al. 2014, *MNRAS*, 441, 2361  
 Viviani, M., Käpylä, M. J., Warnecke, J., Käpylä, P. J., & Rheinhardt, M. 2019, *ApJ*, in press, arXiv:1902.04019  
 Viviani, M., Warnecke, J., Käpylä, M. J., et al. 2018, *A&A*, 616, A160  
 Warnecke, J. 2018, *A&A*, 616, A72  
 Warnecke, J. & Bingert, S. 2019, *Geophysical & Astrophysical Fluid Dynamics*, 0, 1  
 Warnecke, J., Brandenburg, A., & Mitra, D. 2011, *A&A*, 534, A11  
 Warnecke, J., Brandenburg, A., & Mitra, D. 2012, *JSWSC*, 2, A11  
 Warnecke, J., Chen, F., Bingert, S., & Peter, H. 2017, *A&A*, 607, A53  
 Warnecke, J. & Käpylä, M. J. 2019, *A&A*, submitted, arXiv:1910.06776  
 Warnecke, J. & Peter, H. 2019, *A&A*, 624, L12  
 Warnecke, J., Rheinhardt, M., Tuomisto, S., et al. 2018, *A&A*, 609, A51  
 Wright, N. J. & Drake, J. J. 2016, *Nature*, 535, 526  
 Zhang, H., Brandenburg, A., & Sokoloff, D. D. 2014, *ApJ*, 784, L45  
 Zhang, H., Brandenburg, A., & Sokoloff, D. D. 2016, *ApJ*, 819, 146  
 Zhang, H., Sakurai, T., Pevtsov, A., et al. 2010, *MNRAS*, 402, L30